

Power and Control Autonomy for High Speed Locomotion With an Insect-Scale Legged Robot

Benjamin Goldberg^{1*}, Raphael Zufferey^{2*}, Neel Doshi¹, E. Farrell Helbling¹, Griffin Whittredge¹, Mirko Kovac², and Robert J. Wood¹

Abstract—We present a power and control autonomous, insect-scale legged robot, the Harvard Ambulatory MicroRobot with RF communication (HAMR-F). At only 2.8g and 4.5cm in length, HAMR-F is capable of locomotion at speeds up to 17.2cm/s (3.8 body lengths per second) with an onboard battery. Two microcontrollers and custom drive electronics independently control eight high-voltage piezoelectric actuators to enable gait flexibility and maneuverability across a range of stride frequencies. An onboard MEMS IMU provides feedback for controlled, straight-line running on this size- and weight-constrained mobile microrobot. The main contributions of this paper are: 1) the design of lightweight power electronics for independently driving multiple high-voltage (200V) piezoelectric actuators, 2) a detailed characterization of HAMR-F’s speed, maneuverability, and cost of transport, and 3) the integration of an onboard feedback controller for straight-line, high speed running.

Index Terms—Micro/Nano Robots, Legged Robots, HAMR, Piezoelectric actuator, Cockroach

I. INTRODUCTION

INSECT-SCALE robotsⁱ have long been envisioned for applications such as search and rescue and confined environment exploration. To date, three of the smallest power and control autonomous mobile robots are Alice (5g, 2.1 cm), Kilobot (36g 3.3 cm), and Colias (> 10 g, 4 cm) [1], [2], [3]. These robots demonstrate some of the salient challenges for functionality at small scales, such as the availability of off-the-shelf hardware (e.g., DC motors) versus the need for customized components (e.g., drive circuitry). At an even smaller scale, the Robobee (80mg, 3cm), uses custom and off-the-shelf sensors to perform proprio- and extero-ceptive sensing with off-board power and control [4], [5].

Early power and control autonomous versions of the Harvard Ambulatory MicroRobot (HAMR) have been presented in [6], [7]. However, these robots (HAMR3 and HAMR-VP) are severely speed-limited, with maximum speeds of 4.23 cm s^{-1} for open-loop operation and 0.63 cm s^{-1} for closed loop

Manuscript received: September, 10, 2017; Revised December, 2, 2017; Accepted December, 5, 2017.

This paper was recommended for publication by Editor Yu Sun upon evaluation of the Associate Editor and Reviewers’ comments.

¹ Harvard University, The John A. Paulson School of Engineering and Applied Sciences and Wyss Institute for Biologically Inspired Engineering

² Aerial Robotics Laboratory, Department of Aeronautics, Imperial College London

*These authors contributed equally. E-mail: bgoldb11@gmail.com, r.zufferey16@imperial.ac.uk

Digital Object Identifier (DOI): see top of this page.

ⁱDefined as having a characteristic length between 1 and 5cm

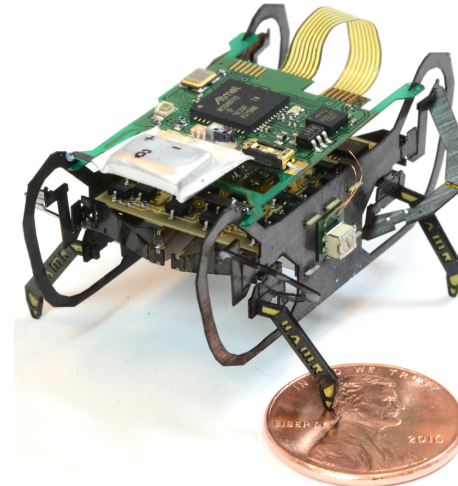


Figure 1. Quadrupedal HAMR-F with custom power and control electronics powered by an 8 mA h lithium polymer battery.

operation. Furthermore, these robots are unable to carry additional payload due to drivetrain limitations and rely on vibratory locomotion (i.e., pseudo-random rather than distinct gait patterns). Consequently, previous versions of HAMR, like the Kilobot and Colias robots, can only operate on flat terrain.

Realizing power and control autonomy for insect-scale robots capable of operation in unstructured environments remains challenging due to inherently high metabolic rates and cost of transport (CoT) [8]. In engineered systems, innovative solutions for energy storage including thin-film batteries, capacitors, and solar arrays have been used to power insect-scale mobile robots [9], [10], [11]. Furthermore, improvements to the net power density of insect-scale systems have been realized by integrating high power density actuators and the necessary drive electronics, such as piezoelectric actuators with a tapped inductor boost converter [12].

In parallel with these advances in actuation, sensing, and energy storage, manufacturing methods for insect-scale devices have also matured sufficiently to enable rapid and reliable assembly of flexure-based mechanisms and piezoelectric actuators [13]. Flexure-based mechanisms are advantageous at this scale as they do not suffer from frictional losses that restrict other actuators and transmissions (e.g. motors and jewel bearings) [14]. Additionally, flexure-based mechanisms benefit from being able to incorporate many degrees-of-freedom (DOFs) into lightweight and compact systems such as a centipede inspired robot [15].

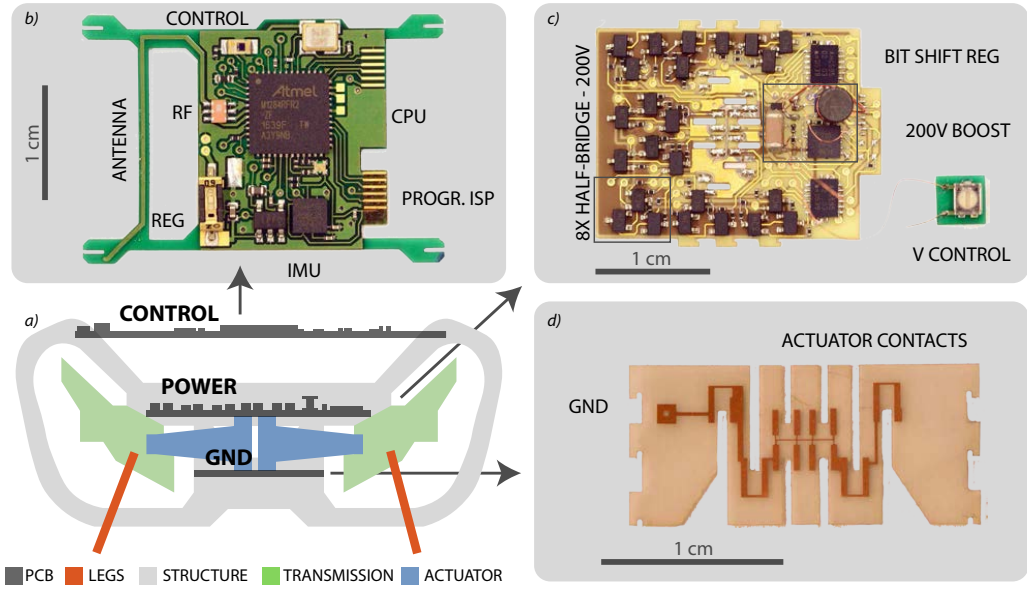


Figure 2. (a) Overall placement of electrical components on HAMR. (b) The control board contains an IMU and high level gait controller, (c) the power board handles high-voltage generation and signal switching, and (d) ground board forms electrical and mechanical connections to the actuators.

In this paper, we describe a new design (HAMR-F, Fig. 1) that leverages advances in manufacturing, sensing, and energy storage to seamlessly integrate the electrical and mechanical components on HAMR. Combined with an upgraded powertrain [16], this results in a more mechanically and electrically robust platform that allows for significantly faster locomotion, variable gait control, improved heading control and payload capacity, and the ability to achieve dynamic gaits with aerial phases (e.g., pronking and jumping).

There are two main sections in this paper. Section II describes the hardware and software architecture of the power circuitry, sensors, and microcontrollers onboard HAMR-F, and Section III describes a detailed performance characterization of HAMR-F. This research lays the groundwork for operation of HAMR and insect-scale legged robots in real-world environments.

II. HARDWARE AND SOFTWARE ARCHITECTURE

HAMR has a 2-DOF spherical five-bar (SFB) transmission that was designed and extensively characterized in [17]. Each SFB is driven by two independently controlled, optimal energy density piezoelectric bimorph bending actuators [18]. One challenge for driving these actuators in an autonomous version of the robot is generating onboard, high-voltage drive signals. Given the current piezoelectric bimorph actuator designs, HAMR requires a minimum power of 100 mW (actuators only) to achieve its fastest speeds at 150 V [17]. Furthermore, in order to maintain independent control of each DOF, eight high-voltage drive signals are required, one for each actuator.

The control and power electronics are separated onto a low-voltage *control board* and a high-voltage *power board* (Fig. 2) to isolate sensitive control components from high-voltage drive components. The circuit boards are professionally manufactured to design specifications (Flex-PCB) and the 0.005" FR4 substrate is machined with a diode-pumped solid

state laser system (Oxford Lasers, E-Series) to interface with the chassis of the robot. The control board interfaces with the high-voltage power board via a custom eight wire flex-connector (DuPont, Pyralux AC 091200EV substrate). It is composed of three low-voltage power lines and three signal lines. The control board (including flex connector) and power board (including transformer) have a mass of 450 mg and 563 mg, respectively. The battery, an 8 mA h lithium polymer (Powerstream, GM300910H), has a mass of 330 mg. A mass distribution is shown in Table I, and the total mass of HAMR-F is 2.79 g. The following sections describe the design and operation of the control and power boards.

Table I
MASS DISTRIBUTION OF HAMR-F

| Component | Mass (mg) |
|---------------|-----------|
| Control Board | 450 |
| Power Board | 563 |
| Transformer | 47 |
| Battery | 330 |
| Actuators | 8×109=872 |
| Chassis | 528 |
| Total Mass | 2790 |

A. Control Board

The control board contains the primary microcontroller (MCU – Atmel, Atmega1284RFR2), the RF transmitter, and the MEMS inertial measurement unit (IMU). The InvenSense MPU-9250 IMU is selected as the best option because of its accurate 9-DOF measurements, I²C communication, and its compact, 3 × 3 × 1mm, footprint. For initial tests, only 1-DOF (yaw) gyroscope measurements are utilized for heading control, and noise estimates are referenced from prior work in Helbling et al. [19]. Future work will develop improved controllers that characterize the noise and incorporate the other sensing modes on the chip.

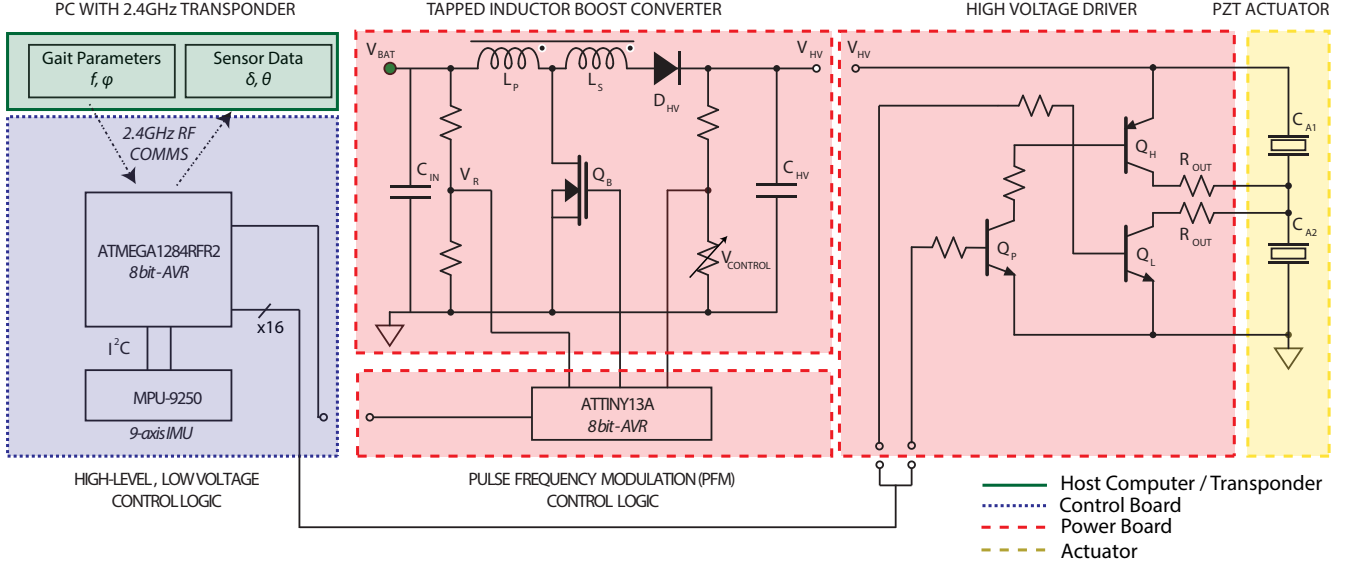


Figure 3. Circuit schematic and system level electronics overview. The host PC (shaded green) manages high level commands that are sent over RF to the control board (shaded blue). Gait and heading control is performed on the control board which sends signals to the power board (shaded red) that performs high-voltage control and drive signal switching. The output mechanical interface is the piezoelectric bimorph bending actuator (shaded yellow).

The ATmega1284RFR2 is RF-enabled, communicating with an offboard, 2.4 GHz transponder connected via serial to a PC. The main program loop in the ATmega performs actuator control and gait timings, and also contains an RF handler and I²C communication with the IMU. The gait cycle runs on an interrupt and maintains 16 transistor states, sending them to a serial to parallel converter on the power board. RF messages enable various operation modes (e.g., changing gait parameters and sending back sensor data).

A trace antenna is integrated onto the control board to minimize the weight for RF communication. The antenna is 31.25 mm long for the 2.4 GHz radio frequency, with the ground plane serving as the other half of the trace antenna. Consistent RF communication at the maximum 45 mW transmission power was observed over a 5 m distance regardless of position, orientation, and partial obstructions (e.g., battery, computers, wires).

B. Power Board

The power board houses all of the high-voltage drive signal components. The high-voltage boost and half-bridge switch topology (Fig. 3) is adapted from Karpelson *et al.* [12]. The hybrid boost converter combines the advantages of a standard boost converter and a flyback converter, namely a small transformer size and a lower voltage on the switching MOSFET (Q_B). The following sections give an overview of the boost circuitry operation and the sizing of the electrical components given HAMR-F's power requirements.

Operation: Figure 4 shows a typical switching cycle of the boost converter. When the MOSFET (Q_B) is switched on and the connection point between the primary and secondary coils is grounded, the current flowing from the power source through the primary coil increases linearly based on the

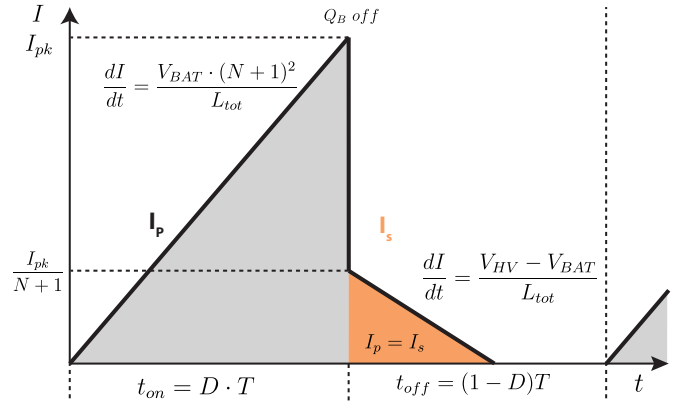


Figure 4. Primary current through the custom transformer over one period in steady-state. In the first phase (gray), charge builds in the primary coil with no charge in the secondary coil. In the second phase (orange), after Q_B is turned off, current discharges through both coils. Figure adapted from [12] and [20].

inductance, L_p . There is no current flow in the secondary coil as it is blocked by the fast-switching diode (D_{HV}).

When Q_B is off, the transformer behaves as an inductor, (L_{tot}), composed of the two windings in series. The charge stored in the primary coil is released and a current flows through the diode to the high-voltage line (V_{HV}). The capacitor on the high-voltage side (C_{HV}) discharges the energy as needed and limits voltage ripple when Q_B is on (t_{on}). The current in the primary coil (I_p) is equal to the current in the secondary (I_s) while Q_B is off and approaches zero as the capacitor is charged. A voltage divider monitors the output voltage (V_R) and a switching cycle is initiated as described below.

Pulse frequency modulation (PFM) is used to vary the

frequency of pulses as needed for the varying output load of the actuators. The PFM is controlled by a dedicated MCU (Atmel, ATtiny13A). The ATtiny13A is the smallest available MCU ($3 \times 3\text{mm}$ QFN10 package) that meets the necessary computational requirements, namely an analog comparator with 8 MHz clock speed for $< 5\text{V}$ ripple for driving the high-voltage circuit. The analog comparator is used to generate a flag when the feedback voltage decreases past the internal bandgap reference voltage of 1.1V. One disadvantage is that the reference voltage is fixed by an internal resistive divider and cannot be altered in software. A potentiometer is included (V_{CONTROL}) so that the feedback voltage can be manually adjusted.

Sizing: Careful sizing of each component in the high-voltage circuit is required. Specifically, the winding ratio (N), the primary and secondary number of turns (N_p, N_s), the PFM duty cycle (D), the maximum voltage on the MOSFET (V_{mos}^{\max}), and the capacitance (C_{HV}) must be considered. The following section describes a physics-based sizing of the standard boost converter (parameters with subscript BST refer to the standard boost circuit, where the transformer is a single inductance).

To minimize component weight, we seek to minimize the inductance, L_{BST} . A guideline to inductor design is given by [21]:

$$L_{\text{BST}} = \frac{V_{\text{BAT}}(V_{\text{HV}} - V_{\text{BAT}})}{\Delta I_L \cdot f \cdot V_{\text{HV}}}, \quad (1)$$

where ΔI_L is the inductor ripple current in a standard boost configuration, f is the switching frequency, and V_{BAT} is the input battery voltage. The inductor ripple current is a design parameter defined as a percentage, K_L , of the inductor current. A typical value for K_L is 40%. Ripple is then calculated as:

$$\Delta I_L = K_L \cdot I_{\text{out,max}} \frac{V_{\text{HV}}}{V_{\text{BAT}}}. \quad (2)$$

In our application, $V_{\text{BAT}} = 4.0\text{V}$, $V_{\text{HV}} = 200\text{V}$, and $I_{\text{out,max}} = 3\text{mA}$, based on the worst-case estimated power of 600 mW for the combined eight drive stages. V_{HV} is measured in the PFM loop at a frequency (f), of 1 MHz. This frequency is close to the maximum speed achievable with the ATtiny and is sufficient for smooth waveform generation at a maximum stride frequency of 34 Hz. Higher frequencies would result in greater MOSFET switching losses and alternating current skin losses. The constraints of Eqs. 1 and 2 set the optimal theoretical boost inductance to be $L_{\text{BST}} = 65\text{ }\mu\text{H}$.

In the hybrid transformer-boost topology, the L_{BST} is replaced by an auto-transformer of equivalent series inductance L_{tot} . This inductance as well as the primary inductance are defined as follows:

$$L_{\text{tot}} = N \cdot L_{\text{BST}} \text{ and } L_p = \frac{L_{\text{BST}}}{N} \quad (3)$$

To calculate these values, the turn ratio, N , needs to be determined. For this, the schematic in Fig. 4 shows the linear discharge to zero from $I_{\text{pk}}/(N + 1)$ during the t_{off} phase of Q_B . Using the maximum output current required in our application, we can determine N as follows from Fig. 4:

$$I_{\text{out,max}} = \frac{V_{\text{BAT}}^2 D^2}{2f \cdot (V_{\text{HV}} - V_{\text{BAT}}) \cdot L_{\text{BST}}} \cdot N. \quad (4)$$

As stated above, the actuation stage requires a maximum of 3 mA on average. Setting $D = 9$ recommended in [12] yields $N \approx 9$. Next, the switching transistor is sized in order to withstand a drain-source voltage given by:

$$V_{\text{mos}}^{\max} = \frac{V_{\text{HV}}}{N + 1}. \quad (5)$$

This voltage is $(N + 1)$ times lower than in a standard boost configuration, which reduces the component size. The number of turns of the primary is calculated using the above inductance value:

$$N_p = \sqrt{\frac{l_{\text{gap}} L_p}{\mu_0 A_c}}, \quad (6)$$

where l_{gap} is the distance the magnetic flux travels across air and A_c is the core cross-sectional area. Air reluctance (μ_0) is significantly higher than ferrite reluctance; therefore, we only need to consider the air gap reluctance. Since the core is not shielded, there is a 1 mm air gap. Solving for N_p yields $N_p \approx 30$ turns. With the turns ratio of 9, the secondary inductance should be approximately 220 μH and the minimum wire gauge for the secondary coil is determined from $I_{\text{max,out}}$. Assuming a current density of 6 A/mm² and a worst-case power draw of 600 mW at 200 V, the secondary coil needs a wire diameter, d_s of at least 25 μm or AWG 50.5.

Finally, for C_{HV} , the storage capacitor needs to source the power for all of the actuators. Given the measured capacitance of 20 nF for a single actuator, C_{HV} should be greater than 160 nF to reduce ripple in the worst case of all actuators switching at once.

C. High-Voltage Half-Bridge Switch

A discrete half-bridge is chosen as a low mass solution to achieve unipolar, high-voltage switching with three bipolar junction transistors (BJT) (Fig. 3). The low side BJT (Q_L) connects the actuators to ground while the high-side BJT (Q_H) connects to V_{HV} . Since the base voltage of the high side BJT needs to be approximately 200 V, it cannot be directly driven by the MCU; therefore, a third transistor (Q_P) is added to drive Q_H . The piezoelectric plates are driven by the two identical high-side and low-side 300 k Ω resistors. This forms an RC low-pass circuit with the capacitive load of the actuator, used to smooth the square wave drive signals. The cutoff frequency is 26.5 Hz based on the capacitance of the actuator (20 nF) and the maximum achievable stride frequency allowed by the MCU (34 Hz).

In order to reduce the number of outputs required from the MCU, a serial to parallel converter is employed to drive the transistor switching for all eight actuators. The 74AHC bit-shift-registers (BSRs) require only three signals – two clocks and one data line – and can output eight digital signals. Two BSRs can be daisy-chained to drive 16 transistors (necessary for the eight actuators).

D. Coil Manufacturing

As of this writing, no off-the-shelf transformer meets the low-mass (< 100 mg) requirements of the robot. Therefore, the transformer is custom wound for this application using a bare ferrite core (Coilcraft, LPS5030). The coil is fabricated based on the calculations in the prior section and the experimentally measured properties of the coil are shown in Table II. Due to size constraints and coil packing, exact turn ratios and inductances varied from the target values.

Table II
TRANSFORMER COIL PARAMETERS

| Parameter | A_c^* | l_{gap}^* | N_p | N | d_p | d_s | L_p | L_s | m_{tot} |
|-----------|-----------------|-------------|-------|-----|-------|-------|-------|-------|-----------|
| Units | mm ² | mm | # | # | AWG | AWG | μH | μH | mg |
| Target | 2.4 | 1 | 30 | 9 | 40 | 50.5 | 8 | 220 | 40 |
| Measured | 2.4 | 1 | 22 | 8.4 | 40 | 50.5 | 11 | 370 | 47 |

*Coilcraft Ferrite Core dimensions

III. RESULTS

HAMR-F shows significant performance improvements over prior versions of HAMR (e.g. [7], [6]), and the following section characterizes its performance. Two different HAMR-F configurations are used for data collection: 1) An “evaluation robot” that has a lightweight tether to a 4.1 V power supply to simulate battery power to rapidly conduct benchmark measurements, and 2) A “full robot” with an onboard, rechargeable battery of varying capacities (8 mA h, 10 mA h, and 25 mA h).

A. Drive Signals and Speed

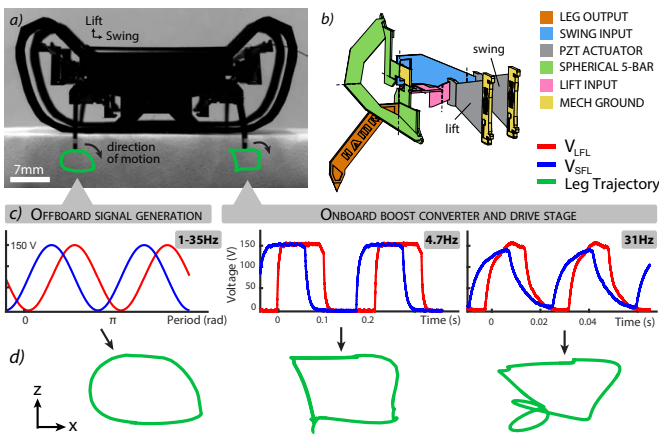


Figure 5. (a) A robot side view illustrates foot trajectories. (b) The leg tip is linked to the actuators and the structure via a spherical five-bar transmission. (c) An idealized sinusoidal drive signal is compared to the onboard drive signals, and (d) the resulting leg trajectories at both 4.7 Hz and 31 Hz, which shows increased rounding of the leg trajectory at 31 Hz compared to 4.7 Hz. Despite variations in the drive signals compared to offboard signal generation and added payload of a battery, the top speed of HAMR-F is only reduced by 14%.

In previous studies, sinusoidal signals were determined to result in the fastest locomotion [17]. This is in contrast to square waves which produce high foot velocities and cause slipping. Therefore, as discussed in Sec. II-C, a resistor in

series with the actuator effectively forms an RC circuit, providing a low-pass filter on the drive signals. The leg trajectories for offboard and onboard signal generation at low (4.7 Hz) and high (31 Hz) stride frequencies are tracked with a camera (Vision Research, v7.3) and are shown in Fig. 5c,d.

Offboard signal generation results in sinusoidal leg trajectories at all tested stride frequencies (up to 35 Hz). Onboard signal generation at low stride frequencies introduces discontinuities and higher harmonics, resulting in leg trajectories that deviate from circular trajectories. However, smoother leg trajectories are restored in air as the stride frequency increase from 4.7 to 30Hz. Furthermore, we hypothesize that running on the ground introduces further damping and filtering, and ultimately results in similar speeds.

Speed of HAMR-F is one of the most significant improvements compared to previous power and control autonomous versions of HAMR. The results of several open-loop speed tests across two gaits and multiple stride frequencies on the full robot are shown in Fig. 6a, and five frames from the supplemental video of HAMR running with the 34 Hz trot are shown in Fig. 6b. Speed tests are run at 160 V for 7 unique stride frequencies, from 4.7-34Hz. Reported speeds are averaged for each stride frequency and gait over n=17 continuous steady-state cycles. The speed of the trot ranges from $2.5\text{-}15\text{ cm s}^{-1}$ and the pronk ranges from $9\text{-}17.2\text{ cm s}^{-1}$. The top speed of 17.2 cm s^{-1} , 3.8 body lengths per second (BL/s), is a 320% increase compared to HAMR3, which was only able to run at 0.9 BL/s. Furthermore, compared to the tethered HAMR-VI which runs at 19.9 cm s^{-1} with a 34 Hz stride frequency, HAMR-F’s top speed is only 14% lower [22].

For quasi-static locomotion, the trot is able to achieve stable locomotion at stride frequencies below 10 Hz. However, of the two tested gaits, a transition to the pronk will result in the fastest locomotion (and lowest CoT) at 34 Hz. Future work will further exploit the ability to vary gait patterns and achieve large aerial phases and dynamic maneuvers, as demonstrated in Goldberg *et al.* [23].

B. Power Consumption and Cost of Transport

The evaluation robot is used to measure the overall input power with the custom transformer coil shown in Table II. Figure 6c shows the power consumption up to the maximum closed-loop stride frequency of 34 Hz and the maximum operating voltage of 200 V. For the operating voltage of 160 V, power ranges from 307-395mW, varying linearly with frequency. Static power board losses at 160 V are approximately 190mW. Since the overhead costs and power board losses are roughly independent of stride frequency, the net efficiency of the robot increases with stride frequency. As described in the following paragraph, this also has the effect of reducing the cost of transport (CoT) with increasing speed.

The power consumption for HAMR at its top speed of 17.2 cm s^{-1} is 395 mW, resulting in a dimensionless CoTⁱⁱ of 83.9. Compared to the lowest CoT for the tethered HAMR-VI (7.4), the CoT for HAMR-F is approximately an order of

ⁱⁱDimensionless cost of transport defined as $\text{CoT} = \frac{P}{mgv}$, where P is input electrical power, m is mass, g is gravity, and v is velocity.

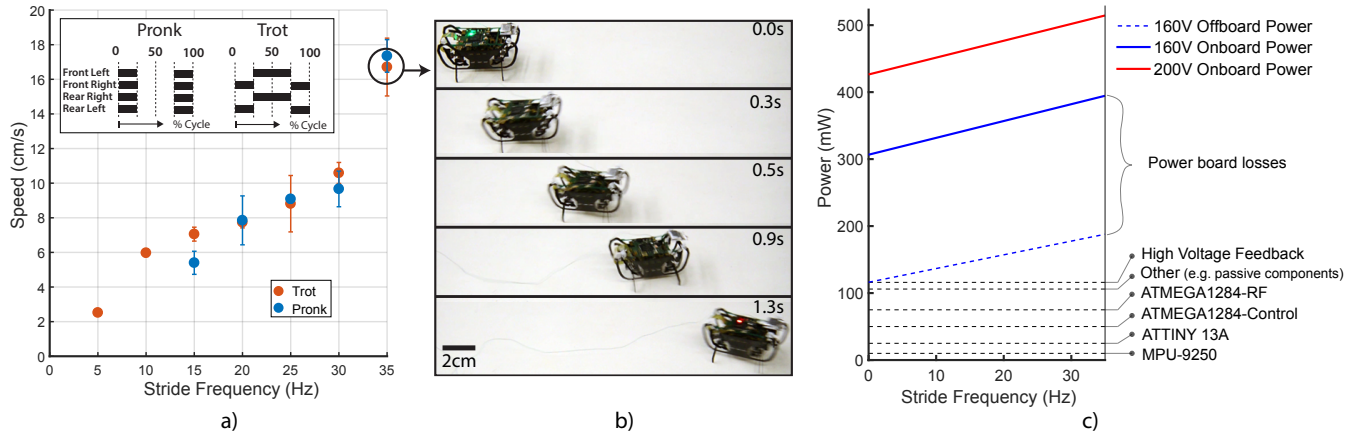


Figure 6. (a) Speed vs. stride frequency for the trot and pronk gaits from 5-34Hz. Each point is the average speed for $n=17$ consecutive cycles with one s.d. error bars. (b) Five frames from the supplemental video of HAMR accelerating from rest with the 34 Hz trot. (c) Power breakdown of HAMR-F. Dashed horizontal lines indicate the cumulative overhead power consumption of the MCU's, sensors, passive components, and high voltage generation. The total overhead power is 116mW. The blue dashed line indicates the total power draw when the eight actuators are connected to offboard commercial piezoelectric drivers (i.e., overhead costs and actuator power). The solid blue and red lines are for onboard actuation at 160 and 200 V, respectively, from 0-34Hz.

magnitude higher. This is due to the overhead control costs, losses in the power board and drive electronics, and high-voltage conversion. The CoT for HAMR-F, however, is only a factor of five higher than similarly-sized insects. For example, the cockroach, *Blaberus discoidalis*, has a mass of 4.0 g, and achieves a CoT of 16.0 at a speed of 10 cm s^{-1} [24]. With improvements to locomotion speed and high-voltage drive, it is possible for the CoT for HAMR to be closer to, or even lower than, the CoT observed in nature.

C. Controller Performance

This section describes maneuverability and control tests performed with the full robot. The MEMS IMU is used to estimate angular velocity, and the gait-agnostic maneuverability scheme implemented offboard in [25] is modified to work with the onboard signal generation of HAMR-F. Open-loop turning rates with HAMR-F are possible up to $\pm 127^\circ/\text{s}$ for the 34 Hz pronk. This rapid turning rate and maneuverability allows for accurate heading control by minimizing angular velocity.

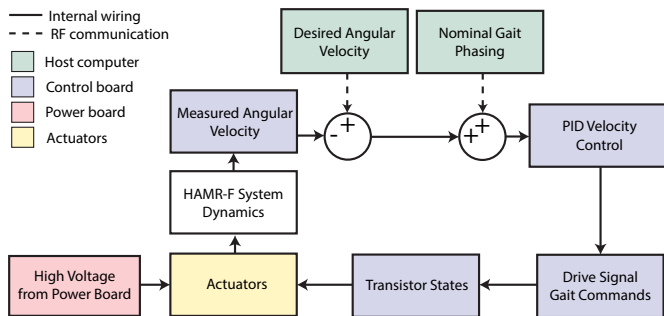


Figure 7. Block diagram of HAMR-F's main MCU during closed loop operation in conjunction with the power board that generates the high-voltage for the actuators. Commands to change gait or heading setpoint can be sent from the host PC to HAMR-F through the RF communication link.

A block diagram of the heading controller is shown in Fig. 7, and the proportional, integral, and derivative gains are

manually tuned to 0.6, 0.02 and 0.005, respectively. There is a significant improvement in the ability to maintain zero average angular velocity, $\bar{\omega}$, with the addition of the feedback controller. Without the controller or any trimming, the robot turns at an average rate of $\bar{\omega} = -0.606$. The average angular velocities for the controlled pronk and trot are $\bar{\omega} = -0.002$ and $\bar{\omega} = -0.008$, respectively (Fig. 8). This corresponds to an RMS heading error of 9.5° and 4.6° for the pronk and trot respectively.

D. Runtime

For the full robot with a 25 mA h lithium polymer battery (PowerStream, PGEB014018), HAMR-F runs for 4.5 minutes at 200 V with a stride frequency of 34 Hz suspended on blocks. After this time, the robot continues to run while the high-voltage slowly drops. A substantial voltage drop below 150 V is observed after actuating the legs for a total of eight minutes. Assuming near top speed ($\sim 15 \text{ cm s}^{-1}$) for 4.5 minutes, this equates to an allowable travel distance of $\sim 40 \text{ m}$.

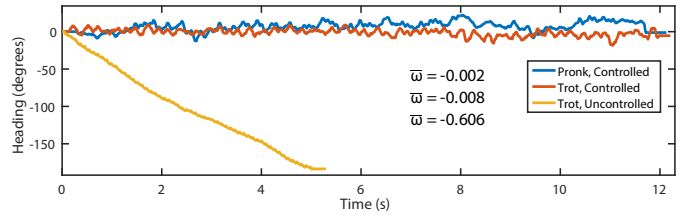


Figure 8. Angular velocity control for the pronk and trot gaits. In the open loop case, there is a consistent drift in the heading. Root mean square heading error for both controlled gaits (pronk and trot) is less than 10° . Open loop conditions are shown in yellow.

IV. CONCLUSIONS AND FUTURE WORK

We presented a major step towards autonomy at the insect-scale by integrating power, control, and communication electronics on a mass- and size-constrained mobile, legged robot. This results in speeds up to 3.8 body lengths per second and

the ability to perform heading control with an RMS error of less than 10° using a MEMS gyroscope.

Future work will focus on integrating additional sensors and performing sensor fusion for more sophisticated state estimation to improve control for use in task-specific applications. Additionally, custom batteries and energy storage options will be considered to extend the range and runtime of HAMR-F. Furthermore, optimizing software and improving the hardware architecture (e.g. incorporating higher performance MCUs) can further improve speed and coverage. For use in performing tasks as a collective, swarms of HAMR-F's can leverage the wireless communication link to communicate between robots, and with a centralized ground station. Finally, future research will explore locomotion in more challenging environments such as in confined spaces or on textured and inclined surfaces.

ACKNOWLEDGEMENTS

Thank you to all members of the Harvard Microrobotics Lab for invaluable discussions. This work is funded by the Wyss Institute for Biologically Inspired Engineering and the National Science Foundation under Grant Number DGE1144152. Any opinion, findings, and conclusions or recommendations expressed in this material are those of the authors and do not necessarily reflect the views of the National Science Foundation. In addition, the prototypes were enabled by equipment supported by the ARO DURIP program (award #W911NF-13-1-0311).

REFERENCES

- [1] G. Caprari, T. Estier, and R. Siegwart, "Fascination of down scalingalice the sugar cube robot," *Journal of micromechatronics*, vol. 1, no. 3, pp. 177–189, 2001.
- [2] M. Rubenstein, C. Ahler, and R. Nagpal, "Kilobot: A low cost scalable robot system for collective behaviors," in *Robotics and Automation (ICRA), 2012 IEEE International Conference on*. IEEE, 2012, pp. 3293–3298.
- [3] F. Arvin, J. Murray, C. Zhang, and S. Yue, "Colias: An autonomous micro robot for swarm robotic applications," *International Journal of Advanced Robotic Systems*, vol. 11, no. 7, p. 113, 2014.
- [4] S. B. Fuller, A. Sands, A. Haggerty, M. Karpelson, and R. J. Wood, "Estimating attitude and wind velocity using biomimetic sensors on a microrobotic bee," in *Robotics and Automation (ICRA), 2013 IEEE International Conference on*. IEEE, 2013, pp. 1374–1380.
- [5] E. F. Helbling, S. B. Fuller, and R. J. Wood, "Altitude estimation and control of an insect-scale robot with an onboard proximity sensor," in *Robotics Research*. Springer, 2018, pp. 57–69.
- [6] A. T. Baisch, C. Heimlich, M. Karpelson, and R. J. Wood, "HAMR3: An autonomous 1.7 g ambulatory robot," in *IEEE/RSJ Intl. Conf. on Intelligent Robots and Systems*. IEEE, 2011, pp. 5073–5079.
- [7] R. Bruhwiler, B. Goldberg, N. Doshi, O. Ozcan, N. Jafferis, M. Karpelson, and R. J. Wood, "Feedback control of a legged microrobot with on-board sensing," in *Intelligent Robots and Systems (IROS), 2015 IEEE/RSJ International Conference on*. IEEE, 2015, pp. 5727–5733.
- [8] R. J. Full, D. A. Zuccarello, and A. Tullis, "Effect of variation in form on the cost of terrestrial locomotion," *Journal of Experimental Biology*, vol. 150, no. 1, pp. 233–246, 1990.
- [9] N. J. Dudney *et al.*, "Thin film micro-batteries," *The Electrochemical Society Interface*, vol. 17, no. 3, p. 44, 2008.
- [10] K. Gilpin, A. Knaian, and D. Rus, "Robot pebbles: One centimeter modules for programmable matter through self-disassembly," in *Robotics and Automation (ICRA), 2010 IEEE International Conference on*. IEEE, 2010, pp. 2485–2492.
- [11] S. Hollar, A. Flynn, C. Bellew, and K. Pister, "Solar powered 10 mg silicon robot," in *Micro Electro Mechanical Systems, 2003. MEMS-03 Kyoto. IEEE The Sixteenth Annual International Conference on*. IEEE, 2003, pp. 706–711.
- [12] M. Karpelson, G.-Y. Wei, and R. J. Wood, "Driving high voltage piezoelectric actuators in microrobotic applications," *Sensors and Actuators A: Physical*, vol. 176, pp. 78–89, 2012.
- [13] J. P. Whitney, P. S. Sreetharan, K. Y. Ma, and R. J. Wood, "Pop-up book MEMS," *Journal of Micromechanics and Microengineering*, vol. 21, no. 11, p. 115021, 2011.
- [14] M. Goldfarb and J. E. Speich, "A well-behaved revolute flexure joint for compliant mechanism design," *Journal of Mechanical Design*, vol. 121, no. 3, pp. 424–429, 1999.
- [15] K. L. Hoffman and R. J. Wood, "Robustness of centipede-inspired millirobot locomotion to leg failures," in *Intelligent Robots and Systems (IROS), 2013 IEEE/RSJ International Conference on*. IEEE, 2013, pp. 1472–1479.
- [16] N. Doshi, B. Goldberg, R. Sahai, N. Jafferis, D. Aukes, and R. Wood, "Model driven design for flexure-based microrobots," in *IEEE/RSJ Intl. Conf. on Intelligent Robots and Systems*, 2015, pp. 4119–4126, <https://doi.org/10.1109/IROS.2015.7353959>.
- [17] A. Baisch, O. Ozcan, B. Goldberg, D. Ithier, and R. Wood, "High speed locomotion for a quadrupedal microrobot," *The International Journal of Robotics Research*, vol. 33, no. 8, pp. 1063–1082, 2014, <https://doi.org/10.1177/027836914521473>.
- [18] N. Jafferis, M. Smith, and R. Wood, "Design and manufacturing rules for maximizing the performance of polycrystalline piezoelectric bending actuators," *Smart Materials and Structures*, vol. 24, no. 6, p. 065023, 2015.
- [19] S. B. Fuller, E. F. Helbling, P. Chirarattananon, and R. J. Wood, "Using a MEMS gyroscope to stabilize the attitude of a fly-sized hovering robot," in *IMAV 2014: International Micro Air Vehicle Conference and Competition 2014, Delft, The Netherlands, August 12-15, 2014*. Delft University of Technology, 2014.
- [20] "Tutorial 1109, small, high-voltage boost converters," Maxim Integrated, Tech. Rep., 2002.
- [21] B. Hauke, "Basic calculation of a boost converter's power stage," Texas Instruments, Tech. Rep., 2014.
- [22] B. Goldberg, N. Doshi, O. Ozcan, and R. J. Wood, "Gait studies on an insect-scale quadruped," in *International Symposium on Adaptive Motion of Animals and Machines (AMAM)*, Cambridge, MA, USA, 2015.
- [23] B. Goldberg, N. Doshi, K. Jayaram, and R. Wood, "Gait studies for a quadrupedal microrobot reveal contrasting running templates in two frequency regimes," *Bioinspiration & biomimetics*, vol. 12, no. 4, 2017, <https://doi.org/10.1088/1748-3190/aa71dd>.
- [24] C. Herreid and R. Full, "Cockroaches on a treadmill: aerobic running," *Journal of insect physiology*, vol. 30, no. 5, pp. 395–403, 1984.
- [25] B. Goldberg, N. Doshi, and R. Wood, "High speed trajectory control using an experimental maneuverability model for an insect-scale legged robot," in *Robotics and Automation (ICRA), 2017 IEEE International Conference on*. IEEE, 2017, pp. 3538–3545, <https://doi.org/10.1109/ICRA.2017.7989405>.